

# Subwavelength Custom Wavefront Shaping by a Nonlinear Electro-optic Spatial Light Modulator

Guillaume Croes,\* Robert Gehlhaar, and Jan Genoe


Cite This: *ACS Photonics* 2024, 11, 529–536


Read Online

ACCESS |

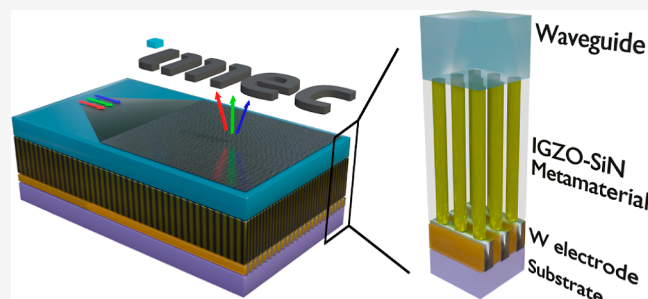
Metrics &amp; More

Article Recommendations

Supporting Information

**ABSTRACT:** Holographic displays offer a method to completely reconstruct any desired wavefront and can thus lead to breakthrough innovation in beamforming, sensing, and information encryption. However, full control over a wavefront in the visible requires features of 100 nm or less. Here, we apply these stringent requirements in an all-encompassing device structure including light source, modulator, and driver electronics. To this end, we propose a continuous electro-optically modulated barium titanate slab waveguide employing a metamaterial cladding layer enabling electrodes to be in contact with the optically active layer. This prevents both the undesired scattering and the absorption that metallic electrodes would introduce. We elaborate the driving requirements of the proposed waveguide display including the optimal use of a nonlinear barium titanate crystal and electrical and optical simulations that show complete control over a waveguided mode, resulting in desired holographic imaging in far-field simulations.

**KEYWORDS:** barium titanate, beam shaping, holography, metamaterial, electro-optic



Downloaded via KU LEUVEN on March 23, 2024 at 19:13:04 (UTC).  
See https://pubs.acs.org/sharingguidelines for options on how to legitimately share published articles.

## INTRODUCTION

Holography was developed by Gabor in 1948 while enhancing the resolving power of an X-ray microscope.<sup>1,2</sup> Since then, his pioneering work has contributed to groundbreaking applications such as computer-generated holograms (CGHs),<sup>3</sup> data storage,<sup>4,5</sup> and interference lithography. In recent years, holography has garnered further interest for its applicability in wavefront shaping, range finding, and optical computing.<sup>6–8</sup> Prominent state-of-the-art technologies that have been used to create holographic devices include spatial light modulators (SLMs) and metasurfaces.<sup>9,10</sup> In general, these devices modulate either the phase, amplitude, or polarization of the incident light to create any wavefront. To date, SLMs have achieved excellent beam steering and image reconstruction using, among other things, phase change materials,<sup>11–13</sup> liquid crystals,<sup>14–17</sup> and acousto-optics to create switchable elements.<sup>18,19</sup> On the other hand, metasurfaces have shown unparalleled control over incident wavefronts by controlling the shape and orientation of subwavelength meta-atoms. Their versatility is further illustrated by the fact that they have shown high-quality holograms<sup>10,20</sup> by employing phase,<sup>21–23</sup> amplitude,<sup>24</sup> and even complex amplitude modulation.<sup>25,26</sup>

Crucially, the attainable steering angle of a holographic display is linked to the employed feature or pixel size and their tunability. Devices ideally have features smaller than the employed wavelength, as this enables steering over a complete 180° range. On the contrary, current state-of-the-art SLMs cannot reduce pixel sizes below several micrometers, leading to

smaller viewing angles and higher-order images. Metasurfaces, on the other hand, approach wavefront shaping from an inverse starting point and always entail subwavelength-sized features drastically increasing the attainable control over any incident wavefront. As such, these devices are capable of projecting zero-order images at large viewing angles and reduced distortion. Unfortunately, at the moment, such metasurfaces typically lack reprogramming capability. Recent work, thus, aims to combine the precise control that subwavelength features offer, together with reprogrammability to create more advanced metasurfaces.<sup>27–30</sup> These so-called metadevices often use materials similar to those of the SLMs mentioned above. However, due to their subwavelength scale, their driving mechanism is now typically plasmonic in nature. Notable examples include phase change materials as active components in plasmonic metal–insulator–metal configurations,<sup>31,32</sup> nanoelectromechanical systems as a modulator of plasmonic resonances,<sup>33,34</sup> and liquid crystal metasurface hybrids.<sup>35</sup> Unfortunately, their tunability remains mostly limited to a complete on–off switch.

These commonly used techniques are often based on the modulation of a free-space beam through either reflection or

Received: September 29, 2023

Revised: January 10, 2024

Accepted: January 22, 2024

Published: February 5, 2024



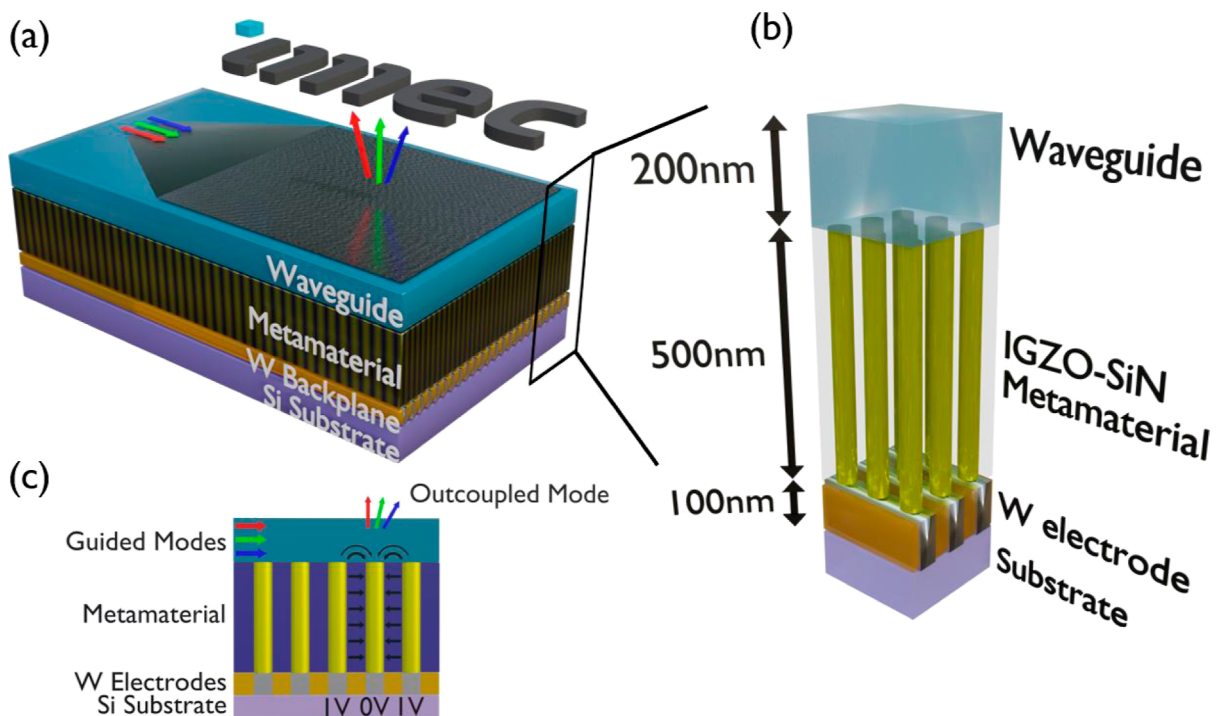


**Figure 1.** (a) Device structure and operation. (b) Enlarged device structure with dimensions true to scale. (c) 2D representation showing device operation on a pixel scale.

transmission. Not surprisingly, this leads to an easier device design since no light source needs to be integrated. However, it also limits their real world applications, requires rigorous alignment, and might thus hinder widespread adoption. More robust and compact devices could be created instead by utilizing a waveguide-based holographic display that includes both a modulator and a light source.<sup>19,36–40</sup> Here, the free-space reference wave and modulated pixels are, respectively, replaced by a waveguided mode and switchable gratings.<sup>41</sup> Several such waveguide holograms have been made throughout the years, but large-scale switchable control over a guided mode remains a challenge. To enable the full potential of a waveguide-based holographic display, three criteria need to be met: (1) a tunable low-loss waveguide and/or cladding layer, (2) large area active control on a subwavelength scale, and (3) a thin-film integrated laser.

To that end, we propose a novel SLM based on an electro-optic barium titanate (BTO) mode coupling waveguide modulated by a metamaterial electrode cladding which consists of a transparent conductive oxide and an index-matched dielectric.<sup>42,43</sup> In doing so, we prevent the periodic pillar array from influencing the BTO waveguide that would occur if it was made from metals and gain the ability to address each pixel separately. Our approach additionally allows decreasing the pixel size below the subwavelength limit to 90 nm which enables precise modulation of the incoming wavefront. This downscaling facilitates the proposed device to reach the quarter wavelength threshold for visible light set forth by Gabor.<sup>2</sup> Holographic projections without higher-order images are made possible as a consequence. By employing fringing electric fields, a drastic increase in control is achieved since modulation can be applied continuously instead of binarily. Furthermore, we opt to use the off-axis component of BTO's electro-optic effect leveraging its mode conversion capabilities and thus reducing noise in comparison to standard mode coupling. Here, we

present a driving scheme inspired by signal analysis that leverages electric field simulations and nonlinear optics such that a completely reprogrammable SLM capable of high-quality beamforming, directional sensing, and complex-amplitude holography can be created in finite-difference time-domain simulations.

## METHODS

**Device Architecture.** The presented device structure has two main components: a cladding electrode enabling sub-wavelength modulation while maintaining high transparency and an actively modulated slab waveguide. The cladding consists of an indium gallium zinc oxide (IGZO) pillar array embedded into a silicon nitride (SiN) matrix that bridges the gap between waveguide and driving electronics. This crucially separates metals 500 nm from the waveguide limiting their adverse effects on the guided mode while simultaneously offering electrical control at 90 nm pitch. In practice, this cladding can be created by etching high aspect ratio holes in a thick SiN layer deposited on a tungsten backplane. Afterward, atomic layer deposition is employed to achieve a conformal IGZO filling. The resulting structure has a thin IGZO surface layer which can be removed through the use of chemical mechanical polishing and a selective SiN etch.<sup>43</sup> Several material systems were considered for the modulated waveguide including liquid crystals, electro-optic crystals ( $\text{LiNbO}_3$ ,  $\text{PbZr}_x\text{Ti}_{1-x}\text{O}_3$ , and  $\text{BaTiO}_3$ ), and thermo-optics. In the end, we opt to use an electro-optic crystal as the inherent size of liquid crystals hampers modulation on a subwavelength scale and a thermo-optic approach would require sufficiently high driving currents to which the electrode cladding is less suited. In particular, BTO seems especially suited for our application as it has shown low-loss waveguides<sup>44</sup> combined with a strong electro-optic response.<sup>45</sup> BTO can be grown by a wide variety of techniques such as molecular beam epitaxy, pulsed laser deposition, and radio frequency sputtering. The

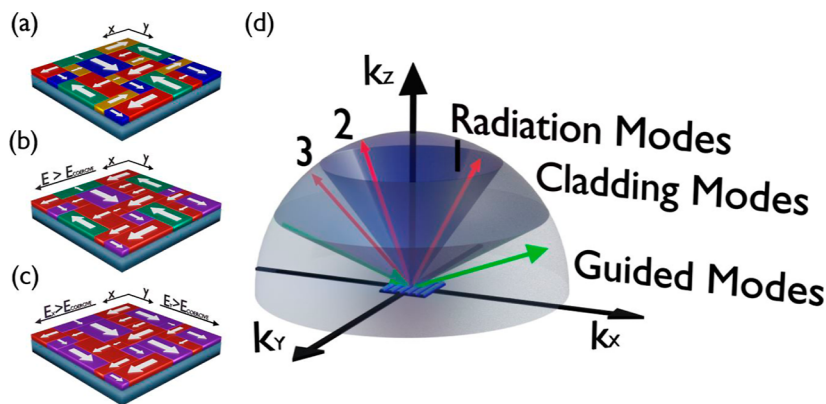


**Figure 2.** (a) BTO wafer with a scrambled domain structure. (b) BTO wafer submitted to an electric field above the coercive field along the  $x$ -axis such that  $x$ -oriented domains align themselves. (c) BTO wafer submitted to a field with components along both the  $x$  and  $y$  axis such that all domains are modulated simultaneously. (d) Wave vector space of the envisioned device having a 400 nm grating-modulated slab waveguide, each conical section represents a different mode regime. The guided mode  $\beta_0$  (green) lies along the  $k_x$  axis, and the grating couples to three modes in total (red). The first two orders couple to a radiation mode, and the third order couples to a cladding mode.

crystalline quality of the material influences the attainable refractive index modulation meaning that epitaxial techniques are preferred.<sup>46</sup> The Pockels effect typically results in refractive index modulation on the scale of  $10^{-3}$  to  $10^{-4}$  and is often used in Q switches or intensity modulators. The resulting low grating diffraction efficiency is, however, no problem in the intended application. In fact, a large area waveguide grating requires sufficiently small modulation, as the guided mode would otherwise quickly lose most of its power. Given that both metamaterial cladding and electro-optical waveguide need to be created separately, thermal bonding will be needed to combine them. Afterward, the carrier wafer of the BTO will need to be removed through chemical mechanical polishing and selective etching.<sup>47</sup>

The device operation together with an enlarged true scale view of a few unit cells and a two-dimensional slice detailing its operation is shown in Figure 1. Under operation, a refractive index modulation pattern based on a CGH can be applied to the waveguide by applying precise voltages to individual pillars. This is similar to the process of write–rewrite in dynamic random-access memory. As a result of the differing pillar voltages, fringing electric fields are formed in the waveguide. Slight disturbances in its refractive index are thus generated, which can cause the light to be coupled out. By adjustment of both the strength of the grating (amplitude modulation) and the period of the grating (phase modulation), it is possible to achieve complex amplitude holography. The device can be thought of as the ultimate implementation of a detour phase (Lohmann) holographic display.<sup>3</sup>

**Electro-optic Behavior of Barium Titanate.** BTO is a perovskite crystal with a  $P4mm$  space group at room temperature that is known for its birefringence and strong electro-optic response. Pockels coefficients as high as 1640 pm/V have been reported, making it an excellent material to be used in electro-optic modulators.<sup>45,48</sup> Due to BTO's birefringent nature, both applied electric field and crystal orientation influence the refractive index. To better comprehend their impact on the refractive index, it is simplest to examine the modulation of the impermeability tensor of a c-oriented BTO crystal, which has its extraordinary axis aligned with the  $z$ -axis. The modulation of the impermeability tensor by the electro-optic effect is typically written as

$$\eta_{ij} = \left( \frac{1}{n^2} \right)_{ij} = \left( \frac{1}{n^2} \right)_{ij}^{(0)} + \sum_k r_{ijk} E_k \quad (1)$$

Here,  $\eta_{ij}$  is the impermeability tensor,  $n$  is the refractive index, and  $r_{ijk}$  is the tensor describing the linear electro-optic effect also called the Pockels coefficients. Since the impermeability tensor is real and symmetric,  $r_{ijk}$  must also be real and symmetric for its first two indices. Consequently, the third rank tensor  $r_{ijk}$  of the linear electro-optic effect can be written as a 2D matrix  $r_{hk}$  in a contracted notation. Furthermore, due to BTO's space group, most Pockels coefficients are zero and because of symmetry coefficients,  $r_{13} = r_{23}$  and  $r_{42} = r_{51}$ . Hence, eq 1 can be simplified to the following

$$\left( \frac{1}{n^2} \right)' = \begin{pmatrix} 1/n_x^2 + r_{13}E_z & 0 & r_{42}E_x \\ 0 & 1/n_y^2 + r_{13}E_z & r_{42}E_y \\ r_{42}E_x & r_{42}E_y & 1/n_z^2 + r_{33}E_z \end{pmatrix} \quad (2)$$

The inverse of the impermeability tensor can now be taken to get the permittivity from which the refractive index and its modulation can be found (see Supporting Information 1). For both in-plane and out-of-plane a-oriented BTO, having their extraordinary axis along the  $x$ - or  $y$ -axis, respectively, eq 2 needs to be modified by an appropriate rotation. Afterward, the effect of an applied field can be calculated by finding the eigenvalues and eigenvectors.

Unfortunately, a-oriented BTO crystals form a scrambled domain structure to alleviate stress resulting in a patchwork of in-plane and out-of-plane BTO that can further align or oppose each other as shown in Figure 2a.<sup>49</sup> These opposing domains, also called antiparallel domains, can be aligned by an electric field above the coercive field, as shown in Figure 2b. Our desired permittivity element for mode conversion is  $\epsilon_{yxy}$  which due to the domain scrambling is modulated by both  $E_x$  and  $E_y$  for out-of-plane BTO and in-plane BTO, respectively (see Supporting Information 2). Both orientations can however supply identical modulation which can be achieved by addressing them at 45° to the crystal orientation. Evidently, this splits the 45° field into  $x$  and  $y$  components for both a-oriented phases, thus resulting in identical modulation. Figure 2c shows the domain structure and how both in-plane and out-of-plane oriented BTO can be

addressed simultaneously. The BTO domain boundaries have a negligible effect on the device performance as a consequence. On the other hand, antiparallel domains result in a phase jump in any applied grating modulation which will disturb the applied signal and locally introduce additional frequencies in the Fourier spectrum of the modulation. Whether this has a significant impact depends on the antiparallel domain size and thus the number of boundaries a waveguide mode has to pass through. Consequently, both crystal growth and crystal poling with the metamaterial cladding layer have a large effect on the device performance.

To prevent degradation of the electro-optic perovskite, both application of excessive electric fields and temperature should be avoided. The first is dependent on the ferroelectric domains and their realignment under an applied electric field. Indeed, this can create significant stress inside the crystal when it is done abruptly and ought to be prevented by proper poling. To that end, gradually increasing the applied bias at a low frequency is preferred. This ensures that domains are poled but crucially gives the crystal time to alleviate stress. In a real-world application, the poling sequence must be run when the device is initialized. The second possible degradation mechanism is tied to the phase change at the Curie temperature of BTO. Here, the crystal loses its ferroelectric and electro-optic behavior. The presented device fortunately requires no current to flow through it, such that the Joule heating is not a concern.

**Mode Conversion.** Mode conversion can be achieved by periodic electro-optic modulation of the BTO waveguide. In eq 2, three separate electro-optic coefficients modulate the impermeability tensor of which  $r_{13}$  and  $r_{33}$  modulate the tensor diagonal and  $r_{42}$  modulates the off-diagonal elements. These coefficients have been reported to be equal to  $r_{13} = 19.5 \text{ pm/V}$ ,  $r_{33} = 97 \text{ pm/V}$ , and  $r_{42} = 1640 \text{ pm/V}$ .<sup>48</sup> For strong modulation, it is best to leverage the off-diagonal elements, which leads to mode conversion. Indeed, where the diagonal elements of the impermeability tensor couple identical electric fields to each other in so-called mode coupling, the off-diagonal elements couple perpendicular electric fields leading to mode conversion. Hence, BTO lends itself extremely well to this due to its strong off-axis Pockels coefficients. We opt to have a TE-guided mode that is converted to a TM radiation mode due to the applied grating, of which the period determines the outcoupling angle. Using the wave vector of the employed modes, mode coupling occurs when the following condition applies

$$\vec{\beta}_r = \vec{\beta}_0 \pm \frac{2\pi n}{\bar{\Lambda}} \quad \text{with } n = 1, 2, 3, \dots \quad (3)$$

Here,  $\vec{\beta}_r$  is the wave vector of the radiation mode,  $\vec{\beta}_0$  is the wave vector on the guided mode, and  $\bar{\Lambda}$  is the grating vector. Figure 2d shows a visual representation of the wavevector space and the influence of an applied grating. In general, a waveguide grating can couple the guided mode with other guided modes, cladding modes, and radiation modes. The number of guided and cladding modes is determined by layer thicknesses and their refractive index meaning that only specific  $\vec{k}_z = \vec{k}_0 - \vec{\beta}_r$  is allowed. Radiation modes on the other hand are unbound such that  $\vec{k}_z$  can take any value. Depending on the chosen crystal orientation, only certain elements of the permittivity matrix (i.e., the inverse of eq 2) can couple the desired modal electric fields. In the coordinate system with mode propagation along the  $x$ -axis, a TE mode has  $(0, E_y, 0)$  as field components while a TM

mode has  $(E_x, 0, E_z)$  components. Hence, for good coupling,  $\epsilon_{yx}$  and  $\epsilon_{yz}$  need to be strongly modulated.

**Grating Reconstruction Using Signal Analysis.** The proposed method relies on an applied waveguide grating to couple out light and create the desired far-field pattern. To that end, the principles of signal analysis can be applied to the sampling and reconstruction of space-varying grating patterns instead of their typical time-based signals. When the Nyquist–Shannon sampling theorem is kept in mind, this allows for the creation of any grating while preserving all information. As a consequence, the calculation of a complex pillar electrode array can ultimately be simplified to the summation of the individual electric fields. The main difference compared to the signal analysis is that the elemental building block is not the Fourier transform of the window function (i.e., a *sinc* function) but the electric field created by a single biased pillar. Consequently, a certain degree of error is expected by employing a nonoptimal reconstruction function.

Finding the required voltage at each pillar of the metamaterial is best done by starting from the desired refractive index. Translating this desired pattern to a set of voltages can be done analytically by first sampling the required refractive index modulation at the period of the electrodes. Afterward, the necessary electric field for the refractive index modulation created between each electrode pair can be found from the Pockels effect. Finally, the simulated electric field can be compared to the desired field to find the voltage for each pillar (see Supporting Information 3).

The required grating is dependent on the intended application. In the case of beam steering, eq 3 together with Snell's law can be used to link the applied period to the outcoupling angle of the radiation mode.<sup>41</sup> For holography, a more advanced grating is required, and two possibilities exist. First, for a point-based hologram, as shown in Figure 4c, a grating is needed that links the outcoupling angle and its accompanying period to the spatial coordinate of the waveguide such that all out-coupled light focuses on a single point. Alternatively, in the case of a phase-map hologram calculated by Gerchberg–Saxton, each waveguide pixel requires an out-coupling grating that yields the correct phase difference. To that end, each pixel row along the propagation direction has to be treated separately. Both holography approaches can be determined starting from the propagation phase-matching condition based on the device geometry of eq 4

$$\phi_1 = \phi_2(x, y) + 2\pi N \quad \text{with } N = 0, 1, 2, \dots \quad (4)$$

In the case of point-based holograms,  $\phi_1$  is the accumulated propagation phase between the image point ( $P_1$ ) and the center  $(x_0, y_0)$  on the hologram plane.  $\phi_2$  consists of two sections. The first section exists between  $(x_0, y_0)$  and any other point  $(x, y)$  on the hologram plane. The second one spans between  $(x, y)$  and the image point  $P_2$  (see Supporting Information 4). For phase-map holograms,  $\phi_1$  is the accumulated phase of the mode between the edge of the waveguide and  $(x, y)$ , and  $\phi_2$  is the desired phase of the out-coupled light at  $(x, y)$ . For both, the slab waveguide grating can be written as

$$\Lambda(x, y) = A(x, y) \cos(\phi_1 - \phi_2(x, y)) \quad (5)$$

Here,  $\Lambda$  represents the desired grating profile,  $A$  is the grating intensity, and the cosine is required to yield the correct period from the desired phase differences (see Supporting Information 4). For focusing on a single point,  $P_1$  and  $P_2$  should be taken to

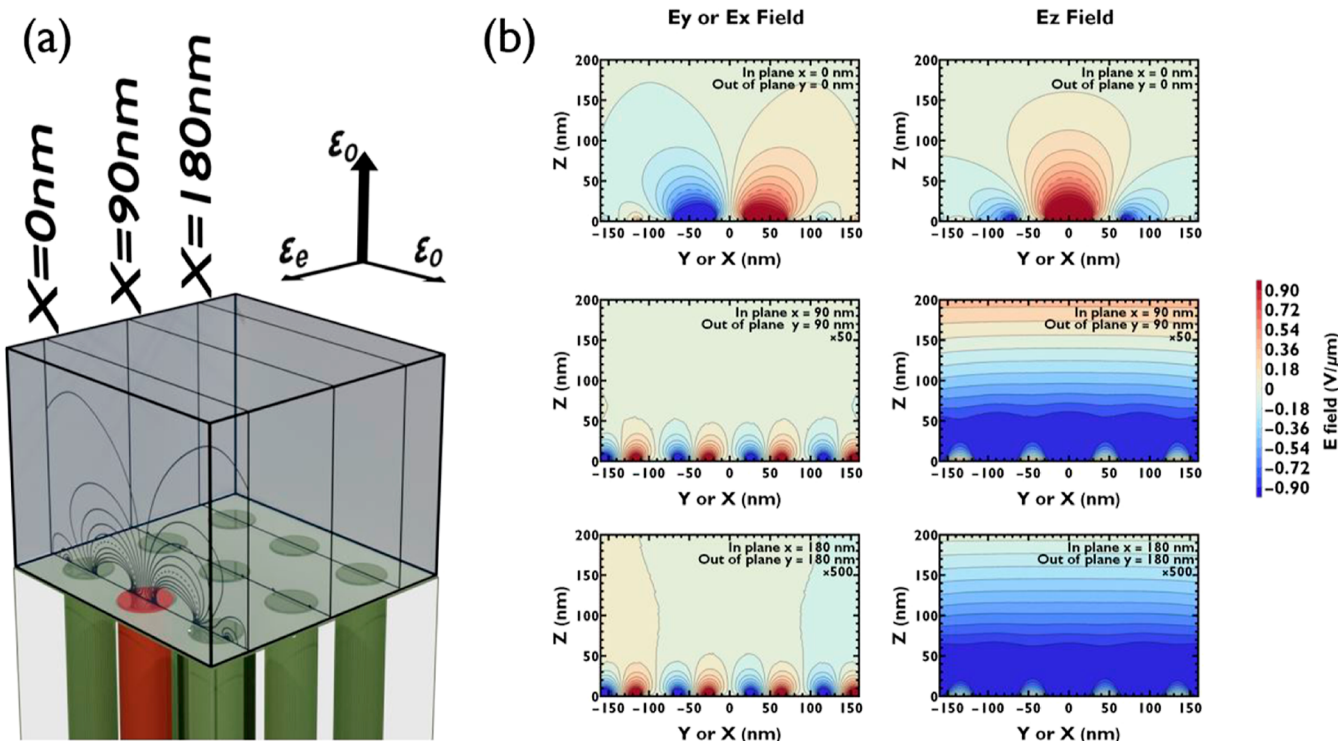


**Figure 3.** (a) Schematic showing the pillar array used in the COMSOL FE simulations, red indicates the biased pillar. The planar slices above indicate the plotted area in (b). (b) Electric field data for both in-plane and out-of-plane, for which  $E_y$  and  $E_x$ , respectively, lead to the desired mode conversion. Due to the  $90^\circ$  rotation between them, both orientations result in an identical electric field along  $90^\circ$  rotated axes.

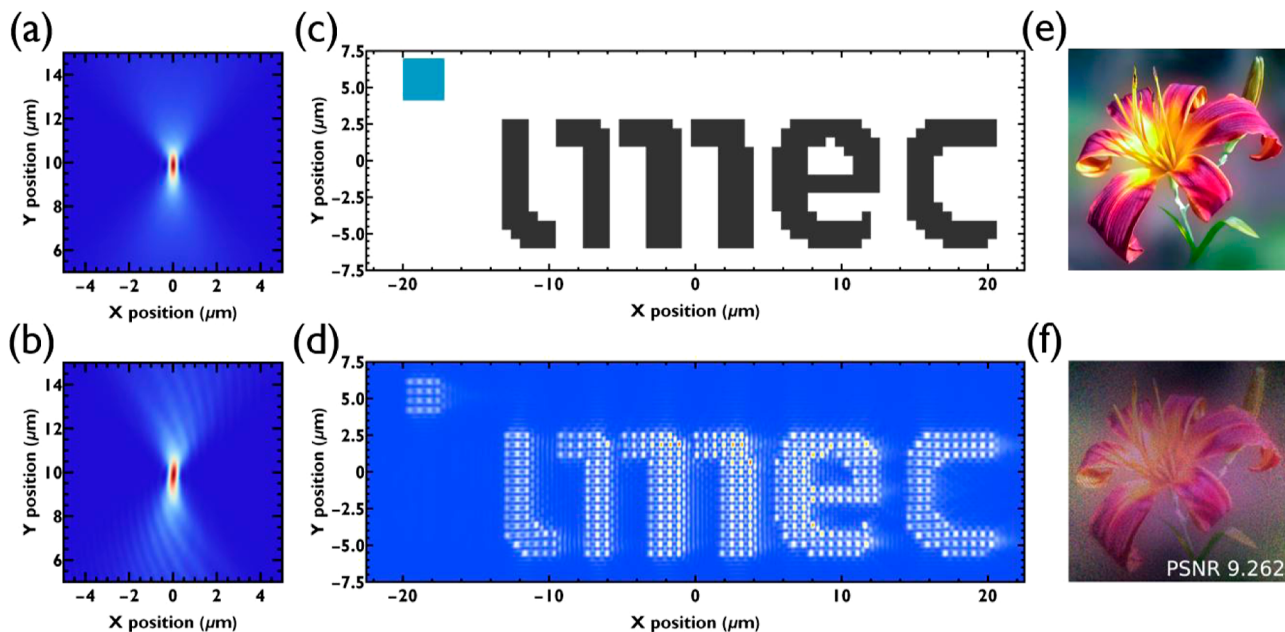


**Figure 4.** (a) Farfield intensity of a focusing spot made in a 2D FDTD simulation using an idealized grating modulation. (b) Farfield intensity plot of a focusing spot created by a grating reconstructed with electric fields. (c) Pixelated imec logo used as a point map for 3D simulations. (d) Superposition of multiple focusing spots, each representing one pixel out of the pixelated imec logo. (e) Flower image used for hologram calculation. (f) Reconstructed flower hologram.

be identical. When additional points need to be imaged,  $\phi_1$  can be kept and  $\phi_2$  should be altered through  $P_2$ . The acquired grating can then be superpositioned on any previous grating to yield multiple focus points.

## RESULTS AND DISCUSSION

**Electric Field Simulations.** Finite element (FE) electric field simulations were done using COMSOL Multiphysics.<sup>50</sup> The relative permittivity of c-oriented BTO was set to  $\epsilon_r = (3600, 3600, 150)$  and was rotated accordingly for the other crystal orientations.<sup>51</sup> The SiN cladding was given a relative

permittivity of  $\epsilon_r = 7$ , the top cladding was air, and the IGZO pillars were excluded as they allow no fields inside, thanks to their conductivity. To avoid dielectric breakthrough, the voltage difference was limited to 0.1 V between adjacent pillars. The influence of the crystal orientation was assessed by simulating a large array of pillars where only the central pillar was biased, leaving the rest grounded. The array size was chosen large enough so that the electric fields from the central pillar nearly vanished (1E6:1) within the simulation range and hence, no edge effects are present in a superposition. Figure 3a shows the center of the performed simulations with the biased pillar indicated in red. The slices indicated in the waveguide represent the planes for which the a-oriented electric fields are plotted in Figure 3b. The simulations indicate that c-oriented BTO does not allow electric fields to penetrate significantly, which is due to the large in-plane and out-of-plane relative permittivity (see Supporting Information 5). Consequently, c-oriented BTO only offers minimal modulation of the guided mode and is thus not an interesting material for a guided-mode SLM. Conversely, both in-plane and out-of-plane BTO allow large electric fields to exist deep in the waveguide as is evident from Figure 3b. To our benefit, the electric fields remain rather confined as a result of the large relative permittivity of BTO making electric field superpositions easier since only few neighboring pillars need to be included before fields decay to negligible values. Both 2D and 3D electric fields for various crystal orientations can be found in data set 1.<sup>52</sup>

**Optical Simulations.** Finite-difference time-domain simulations in 2D and 3D were performed in Lumerical FDTD.<sup>53</sup> In each, the near field was recorded and subsequently used for a far-field projection. 2D simulations were set up to observe the difference between a grating reconstructed by superpositioning electric fields and its idealized counterpart (i.e., eq 5). Here, both phase (grating period) and amplitude modulation (grating strength) combine to yield accurate focusing. Figure 4a,b shows an example where the guided mode focuses 10  $\mu\text{m}$  above the slab waveguide surface. In both cases, the waveguide was 50  $\mu\text{m}$  long and the wavelength was 550 nm. Looking at the focusing quality for both, we conclude that the electric field-based grating matches its ideal case very well. This result confirms the idea that reconstructing a signal using a nonoptimal window function, namely, the electric field of a single biased pillar electrode, provides accurate reconstructions of the desired modulation. Notably, the out-coupled intensity in Figure 4b seems slightly rotated which is attributed to a higher degree of outcoupling and accompanying higher refractive index modulation likely caused by the sampled points aligning better with the grating maxima. This is no surprise since the required grating periods are significantly larger at the left side of the focusing spot and the mode propagates from left to right. Here, steering only requires slight modulation of the waveguide mode compared to the right side, where the grating needs to be small enough to steer the mode in an opposite direction. Note that there is no constraint on the focusing distance, and as such, near-field imaging is possible.

Similar simulations were performed in 3D by employing idealized gratings without electric fields to speed up calculations. Compared to the 2D results, this simulation better mimics the device operation, as it requires steering from a slab with the grating vector in the  $xy$ -plane. First, the imec logo was downscaled to have 100 by 50 pixels, as shown in Figure 4c. A waveguide hologram was subsequently created by superpositioning eq 5 with each logo point spaced 610 nm apart.

The simulation area was 50 by 50  $\mu\text{m}$  and the wavelength was 550 nm. To increase the point density, each nearest neighbor was assumed to have a  $\pi$ -phase difference, mimicking interference lithography. The image plane was taken to be 10  $\mu\text{m}$  above the waveguide surface. No points were placed along the symmetry axis of the slab, as steering to these axes requires only one grating component. This translates into a stronger coupling coefficient and individual points overshooting the entire superposition. We find that the superpositioned logo in 3D, as shown in Figure 4d, matches expectations very well since every single point can be identified. Afterward, a more advanced image was created employing a CGH. To that end, a 500 by 500 pixel-sized flower image, as shown in Figure 4e, was first split into its red-green-blue (RGB) channels after which a phase map was calculated for each using the standard Gerchberg–Saxton (GS) algorithm.<sup>54</sup> These phase maps were subsequently imported in Lumerical FDTD and used to create the required waveguide grating for the three separate holograms by subtracting the phase that the traveling guided mode accumulates between individual pixels. Blue light was equated to 465 nm, green light was equated to 550 nm, and red light was equated to 640 nm. Care was taken in the GS algorithm and a subwavelength-corrected far-field calculation based on the Rayleigh–Sommerfeld (RS) diffraction integral was used to negate the distortion that the Fresnel approximation typically introduces for such pixels.<sup>55</sup> A consequence of the single Fourier transform RS propagation is that the employed pixel size also influences the image size through

$$d_{\text{im}} = \frac{\lambda D}{d_{\text{pix}}} \quad (6)$$

Here,  $d_{\text{im}}$  is the image size,  $\lambda$  is the employed wavelength,  $D$  is the imaging distance, and  $d_{\text{pix}}$  is the pixel size. Hence, 180 nm was chosen to be the pixel size of the blue channel, which is the size of the smallest attainable grating period. Both pixel sizes for green and red were chosen such that an identical image size was attained in the far-field. At a distance of 10 cm, these are 212.9 and 247.7 nm, respectively, which leads to an image size of 25.83 cm. Incidentally, the simulation area varied accordingly from 90 by 90  $\mu\text{m}$  to 106 by 106  $\mu\text{m}$  and 124 by 124  $\mu\text{m}$ . Afterward, the Lumerical far-field was extracted for each and recombined to yield Figure 4f. The recombined image yields an accurate reconstruction of the desired image, although some speckle is visible. More advanced versions of the GS algorithm can be employed to reduce the present speckle. A peak signal-to-noise ratio (PSNR) of 9.262 was attained for the recombined RGB image. We find that the blue channel attains the best PSNR whereas the red channel attains the lowest (see Supporting Information 6).

## CONCLUSIONS

We propose a novel approach to beam shaping and holography that leverages the subwavelength features of a metamaterial, the fast tunability of electro-optic modulators, and the function reconstruction of the signal analysis. A birefringent perovskite BTO slab is used as active material, meaning that the waveguide dynamics allow for mode conversion between TE and TM modes reducing the outcoupling noise. Moreover, the device architecture enables complex amplitude modulation of the waveguide, since both the grating period (phase modulation) and the modulation strength (amplitude modulation) are adjustable. We give insights into the BTO electro-optic driving

by highlighting its crystal dynamics and simulating electric fields for various crystal orientations. We additionally present the grating requirements for efficient and precise coupling of a single focusing point. Finally, the presented theoretical considerations were utilized in optical FDTD simulations and show that an excellent BTO-based beam-shaping device can be created. First, through a hologram grating that creates a single focusing point, the same pattern was employed in a point-based hologram. To demonstrate the versatility of the method, the same concepts were furthermore applied to a CGH split in its RGB channels and attained a PSNR of 9.262. Both 3D holograms result in accurate depictions of the intended image.

## ASSOCIATED CONTENT

### Data Availability Statement

The 3D electric field data extracted from the COMSOL Multiphysics simulations employed in this study are available in data set 1.<sup>52</sup>

### Supporting Information

The Supporting Information is available free of charge at <https://pubs.acs.org/doi/10.1021/acsphtronics.3c01401>.

Inverse of the impermeability tensor for c-oriented and both a-oriented BTO phases, effect of antiparallel domains on the electro-optic modulation, phase grating reconstruction, derivation of a waveguide focusing grating, COMSOL electric field simulations for c-oriented BTO, and details on PSNR of hologram channels ([PDF](#))

## AUTHOR INFORMATION

### Corresponding Author

Guillaume Croes – Electrical Engineering Dept. (ESAT), KUL, Leuven 3001, Belgium;  [orcid.org/0000-0001-6168-9794](http://orcid.org/0000-0001-6168-9794); Email: [Guillaume.Croes@imec.be](mailto:Guillaume.Croes@imec.be)

### Authors

Robert Gehlhaar – Sensors and Actuators Technology (SAT), Imec, Leuven 3001, Belgium

Jan Genoe – Sensors and Actuators Technology (SAT), Imec, Leuven 3001, Belgium; Electrical Engineering Dept. (ESAT), KUL, Leuven 3001, Belgium;  [orcid.org/0000-0002-4019-5979](http://orcid.org/0000-0002-4019-5979)

Complete contact information is available at:

<https://pubs.acs.org/10.1021/acsphtronics.3c01401>

### Funding

This work has received funding from the European Research Council (ERC) under the European Union's Horizon 2020 research and innovation program (grant agreement no. 742299). G.C. has received an SB PhD fellowship from the FWO (application no. 1S91520N).

### Notes

The authors declare no competing financial interest.

## REFERENCES

- (1) Gabor, D. A New Microscopic Principle. *Nature* **1948**, *161*, 777–778.
- (2) Gabor, D. Holography, 1948–1971. *Science* **1972**, *177*, 299–313.
- (3) Brown, B. R.; Lohmann, A. W. Complex Spatial Filtering with Binary Masks. *Appl. Opt.* **1966**, *5*, 967.
- (4) van Heerden, P. J. Theory of Optical Information Storage in Solids. *Appl. Opt.* **1963**, *2*, 393.
- (5) Boj, S.; Pauliat, G.; Roosen, G. Dynamic holographic memory showing readout, refreshing, and updating capabilities. *Opt. Lett.* **1992**, *17*, 438.
- (6) Wei, Q.; Huang, L.; Zentgraf, T.; Wang, Y. Optical wavefront shaping based on functional metasurfaces. *Nanophotonics* **2020**, *9*, 987–1002.
- (7) Ambs, P. Optical Computing: A 60-Year Adventure. *Advances in Optical Technologies* **2010**, *2010*, 1–15.
- (8) Lugt, A. Signal detection by complex spatial filtering. *IEEE Trans. Inf. Theor.* **1964**, *10*, 139–145.
- (9) Ni, X.; Kildishev, A. V.; Shalaev, V. M. Metasurface holograms for visible light. *Nat. Commun.* **2013**, *4*, 2807.
- (10) Jiang, Q.; Jin, G.; Cao, L. When metasurface meets hologram: principle and advances. *Adv. Opt. Photon.* **2019**, *11*, 518.
- (11) Feinleib, J.; Deneufville, J.; Moss, S. C.; Ovshinsky, S. R. Rapid reversible light-induced crystallization of amorphous semiconductors. *Appl. Phys. Lett.* **1971**, *18*, 254–257.
- (12) Lee, S.-Y.; Kim, Y.-H.; Cho, S.-M.; Kim, G. H.; Kim, T.-Y.; Ryu, H.; Kim, H. N.; Kang, H. B.; Hwang, C.-Y.; Hwang, C.-S. Holographic image generation with a thin-film resonance caused by chalcogenide phase-change material. *Sci. Rep.* **2017**, *7*, 41152.
- (13) Kim, Y.-H.; Cho, S. M.; Choi, K.; Hwang, C. Y.; Kim, G. H.; Cheon, S.; Hwang, C.-S. Crafting a 15 μm pixel pitch spatial light modulator using Ge<sub>2</sub>Sb<sub>2</sub>Te<sub>5</sub> phase change material [Invited]. *J. Opt. Soc. Am. A* **2019**, *36*, D23.
- (14) Fukushima, S.; Kurokawa, T.; Ohno, M. Real-time hologram construction and reconstruction using a high-resolution spatial light modulator. *Appl. Phys. Lett.* **1991**, *58*, 787–789.
- (15) Maeno, K.; Fukaya, N.; Nishikawa, O.; Sato, K.; Honda, T. Electro-holographic display using 15mega pixels LCD. *Practical Holography X*, 1996; pp 15–23.
- (16) Michalkiewicz, A.; Kujawinska, M.; Kozacki, T.; Wang, X.; Bos, P. J. Holographic three-dimensional displays with liquid crystal on silicon spatial light modulator. *Interferometry XII: Techniques and Analysis*, 2004; p 85.
- (17) Kozacki, T. Holographic display with tilted spatial light modulator. *Appl. Opt.* **2011**, *50*, 3579–3588.
- (18) St. Hilaire, P.; Benton, S. A.; Lucente, M. Synthetic aperture holography: a novel approach to three-dimensional displays. *J. Opt. Soc. Am. A* **1992**, *9*, 1969.
- (19) Smalley, D. E.; Smithwick, Q. Y.; Bove, V. M.; Barabas, J.; Jolly, S. Anisotropic leaky-mode modulator for holographic video displays. *Nature* **2013**, *498*, 313–317.
- (20) Zhao, R.; Huang, L.; Wang, Y. Recent advances in multi-dimensional metasurfaces holographic technologies. *PhotonX* **2020**, *1*, 20.
- (21) Huang, L.; Chen, X.; Mühlenbernd, H.; Zhang, H.; Chen, S.; Bai, B.; Tan, Q.; Jin, G.; Cheah, K.-W.; Qiu, C.-W.; Li, J.; Zentgraf, T.; Zhang, S. Three-dimensional optical holography using a plasmonic metasurface. *Nat. Commun.* **2013**, *4*, 2808.
- (22) Devlin, R. C.; Khorasaninejad, M.; Chen, W. T.; Oh, J.; Capasso, F. Broadband high-efficiency dielectric metasurfaces for the visible spectrum. *Proc. Natl. Acad. Sci. U.S.A.* **2016**, *113*, 10473–10478.
- (23) Balthasar Mueller, J.; Rubin, N. A.; Devlin, R. C.; Groever, B.; Capasso, F. Metasurface Polarization Optics: Independent Phase Control of Arbitrary Orthogonal States of Polarization. *Phys. Rev. Lett.* **2017**, *118*, 113901.
- (24) Xu, Z.; Huang, L.; Li, X.; Tang, C.; Wei, Q.; Wang, Y. Quantitatively Correlated Amplitude Holography Based on Photon Sieves. *Adv. Opt. Mater.* **2020**, *8*, 1901169.
- (25) Wang, Q.; Zhang, X.; Xu, Y.; Gu, J.; Li, Y.; Tian, Z.; Singh, R.; Zhang, S.; Han, J.; Zhang, W. Broadband metasurface holograms: toward complete phase and amplitude engineering. *Sci. Rep.* **2016**, *6*, 32867.
- (26) Lee, G. Y.; Yoon, G.; Lee, S. Y.; Yun, H.; Cho, J.; Lee, K.; Kim, H.; Rho, J.; Lee, B. Complete amplitude and phase control of light using broadband holographic metasurfaces. *Nanoscale* **2018**, *10*, 4237–4245.
- (27) Cui, T.; Bai, B.; Sun, H. Tunable Metasurfaces Based on Active Materials. *Adv. Funct. Mater.* **2019**, *29*, 1806692.

- (28) He, Q.; Sun, S.; Zhou, L. Tunable/Reconfigurable Metasurfaces: Physics and Applications. *Research* **2019**, *2019*, 1–16.
- (29) Hu, J.; Bandyopadhyay, S.; Liu, Y.-h.; Shao, L.-y. A Review on Metasurface: From Principle to Smart Metadevices. *Front. Phys.* **2021**, *8*, 502.
- (30) Badloe, T.; Lee, J.; Seong, J.; Rho, J. Tunable Metasurfaces: The Path to Fully Active Nanophotonics. *Advanced Photonics Research* **2021**, *2*, 2000205.
- (31) Li, J.; Kamin, S.; Zheng, G.; Neubrech, F.; Zhang, S.; Liu, N. Addressable metasurfaces for dynamic holography and optical information encryption. *Sci. Adv.* **2018**, *4*, 1–7.
- (32) Zhang, M.; Pu, M.; Zhang, F.; Guo, Y.; He, Q.; Ma, X.; Huang, Y.; Li, X.; Yu, H.; Luo, X. Plasmonic Metasurfaces for Switchable Photonic Spin-Orbit Interactions Based on Phase Change Materials. *Advanced Science* **2018**, *5*, 1800835.
- (33) Zhu, W. M.; Liu, A. Q.; Zhang, X. M.; Tsai, D. P.; Bourouina, T.; Teng, J. H.; Zhang, X. H.; Guo, H. C.; Tanoto, H.; Mei, T.; Lo, G. Q.; Kwong, D. L. Switchable Magnetic Metamaterials Using Micro-machining Processes. *Adv. Mater.* **2011**, *23*, 1792–1796.
- (34) Ren, Z.; Chang, Y.; Ma, Y.; Shih, K.; Dong, B.; Lee, C. Leveraging of MEMS Technologies for Optical Metamaterials Applications. *Adv. Opt. Mater.* **2020**, *8*, 1900653.
- (35) Atorf, B.; Mühlenbernd, H.; Muldarisnur, M.; Zentgraf, T.; Kitzerow, H. Electro-optic tuning of split ring resonators embedded in a liquid crystal. *Opt. Lett.* **2014**, *39*, 1129.
- (36) Sun, J.; Timurdogan, E.; Yaacobi, A.; Hosseini, E. S.; Watts, M. R. Large-scale nanophotonic phased array. *Nature* **2013**, *493*, 195–199.
- (37) Vercruyssse, D.; Mukund, V.; Jansen, R. A.; Stahl, R.; Van Dorpe, P.; Lagae, L.; Rottenberg, X. Density controlled nanophotonic waveguide gratings for efficient on-chip out-coupling in the near field (Conference Presentation). *Silicon Photonics and Photonic Integrated Circuits V* 2016; p 9.
- (38) Huang, Z.; Marks, D. L.; Smith, D. R. Out-of-plane computer-generated multicolor waveguide holography. *Optica* **2019**, *6*, 119.
- (39) Liu, Y.; Shi, Y.; Wang, Z.; Li, Z. On-Chip Integrated Metasystem with Inverse-Design Wavelength Demultiplexing for Augmented Reality. *ACS Photonics* **2023**, *10*, 1268–1274.
- (40) Ding, Y.; Chen, X.; Duan, Y.; Huang, H.; Zhang, L.; Chang, S.; Guo, X.; Ni, X. Metasurface-Dressed Two-Dimensional on-Chip Waveguide for Free-Space Light Field Manipulation. *ACS Photonics* **2022**, *9*, 398–404.
- (41) Croes, G.; Smolentsev, N.; Wang, T. H.; Gehlhaar, R.; Genoe, J. Non-linear electro-optic modelling of a Barium Titanate grating coupler. *Optical Modeling and Performance Predictions XI*, 2020; p 11.
- (42) Croes, G.; Gehlhaar, R.; Genoe, J. Sub-wavelength custom reprogrammable active photonic platform for high-resolution beam shaping and holography. *Active Photonic Platforms (APP)*, 2022; p 84.
- (43) Croes, G.; Puybaret, R.; Bogdanowicz, J.; Celano, U.; Gehlhaar, R.; Genoe, J. Photonic metamaterial with a subwavelength electrode pattern. *Appl. Opt.* **2023**, *62*, F14.
- (44) Eltes, F.; Caimi, D.; Fallegger, F.; Sousa, M.; O'Connor, E.; Rossell, M. D.; Offrein, B.; Fompeyrine, J.; Abel, S. Low-Loss BaTiO<sub>3</sub>–Si Waveguides for Nonlinear Integrated Photonics. *ACS Photonics* **2016**, *3*, 1698–1703.
- (45) Abel, S.; Eltes, F.; Ortmann, J. E.; Messner, A.; Castera, P.; Wagner, T.; Urbonas, D.; Rosa, A.; Gutierrez, A. M.; Tulli, D.; et al. Large Pockels effect in micro- and nanostructured barium titanate integrated on silicon. *Nat. Mater.* **2019**, *18*, 42–47.
- (46) Kormondy, K. J.; Popoff, Y.; Sousa, M.; Eltes, F.; Caimi, D.; Rossell, M. D.; Fiebig, M.; Hoffmann, P.; Marchiori, C.; Reinke, M.; Trassin, M.; Demkov, A. A.; Fompeyrine, J.; Abel, S. Microstructure and ferroelectricity of BaTiO<sub>3</sub> thin films on Si for integrated photonics. *Nanotechnology* **2017**, *28*, 075706.
- (47) Shen, Ya.; Ebadi, S.; Wahid, P.; Gong, X. Tunable and flexible Barium Strontium Titanate (BST) varactors on Liquid Crystal Polymer (LCP) substrates. *IEEE/MTT-S International Microwave Symposium Digest*, 2012; pp 1–3.
- (48) Boyd, R. W. *Nonlinear Opt.*; Elsevier, 2003; pp 485–513.
- (49) Rabe, K. M.; Dawber, M.; Lichtensteiger, C.; Ahn, C. H.; Triscone, J.-M. *Physics of Ferroelectrics*; Springer Berlin Heidelberg: Berlin, Heidelberg, 2007; Vol. 105, pp 1–30.
- (50) COMSOL Multiphysics. v. 6.1. [www.comsol.com](http://www.comsol.com).
- (51) Merz, W. J. The Electric and Optical Behavior of BaTiO<sub>3</sub> Single-Domain Crystals. *Phys. Rev.* **1949**, *76*, 1221–1225.
- (52) Croes, G.; Gehlhaar, R.; Genoe, J. COMSOL Fringing Electric Fields in Barium Titanate, 2024. [https://figshare.com/articles/dataset/COMSOL\\_Fringing\\_Electric\\_Fields\\_in\\_Barium\\_Titanate/24943233](https://figshare.com/articles/dataset/COMSOL_Fringing_Electric_Fields_in_Barium_Titanate/24943233) (accessed Jan 4, 2024).
- (53) Lumerical Inc. <https://www.lumerical.com/> (accessed Sept 28, 2023).
- (54) Gerchberg, R. W.; Saxton, W. O. A Practical Algorithm for the Determination of Phase from Image and Diffraction Plane Pictures. *Optik* **1972**, *35*, 237–246.
- (55) Pang, H.; Yin, S.; Deng, Q.; Qiu, Q.; Du, C. A novel method for the design of diffractive optical elements based on the Rayleigh–Sommerfeld integral. *Opt. Laser. Eng.* **2015**, *70*, 38–44.